Multi-Part Modeling and Segmentation of Left Atrium in C-Arm CT for Image-Guided Ablation of Atrial Fibrillation

Yefeng Zheng*, Dong Yang, Matthias John, and Dorin Comaniciu

***Abstract*—As a minimally invasive surgery to treat atrial fibrillation (AF), catheter based ablation uses high radio-frequency energy to eliminate potential sources of abnormal electrical events, especially around the ostia of pulmonary veins (PV). Fusing a patient-specific left atrium (LA) model (including LA chamber, appendage, and PVs) with electro-anatomical maps or overlaying the model onto 2-D real-time fluoroscopic images provides valuable visual guidance during the intervention. In this work, we present a fully automatic LA segmentation system on nongated C-arm computed tomography (C-arm CT) data, where thin boundaries between the LA and surrounding tissues are often blurred due to the cardiac motion artifacts. To avoid segmentation leakage, the shape prior should be exploited to guide the segmentation. A single holistic shape model is often not accurate enough to represent the whole LA shape population under anatomical variations, e.g., the left common PVs vs. separate left PVs. Instead, a part based LA model is proposed, which includes the chamber, appendage, four major PVs, and right middle PVs. Each part is a much simpler anatomical structure compared to the holistic one and can be segmented using a model-based approach (except the right middle PVs). After segmenting the LA parts, the gaps and overlaps among the parts are resolved and segmentation of the ostia region is further refined. As a common anatomical variation, some patients may contain extra right middle PVs, which are segmented using a graph cuts algorithm under the constraints from the already extracted major right PVs. Our approach is computationally efficient, taking about 2.6 s to process a volume with $256 \times 256 \times 245$ voxels. Experiments on 687 C-arm CT datasets demonstrate its robustness and state-of-the-art segmentation accuracy.**

***Index Terms*—Atrial fibrillation ablation, C-arm CT, left atrial appendage segmentation, left atrium modeling and segmentation, pulmonary vein segmentation.**

I. Introduction

AFFECTING more than three million people in the USA [1], atrial fibrillation (AF) is the most common cardiac arrhythmia (irregular heart beats). AF is associated with an increased risk of stroke, heart failure, cognitive dysfunction, and reduced quality of life, etc. For example, AF patients have a five-fold increased risk of stroke compared to those without AF and about 15%–20% of strokes (which is the third leading cause of death in the USA) can be attributed to AF [2]. As a widely used minimally invasive surgery to treat AF, the catheter based ablation procedure uses high radio-frequency energy to eliminate the sources of ectopic foci. With the improvement in the ablation technology, this procedure was adopted quickly with 15% annual increase rate from 1990 to 2005 [3]. The latest estimate of the number of ablations is approximately 50 000/year in the USA and 60 000/year in Europe [4]. Ablation is mainly performed inside the left atrium (LA), especially around the ostia of the pulmonary veins (PV). Automatic segmentation of the LA has important applications in preoperative assessment and intra-operative guidance for the ablation procedure [5]–[7]. However, there are large variations in the PV drainage patterns [8]. Majority of the population have two separate PVs on each side of the LA chamber, namely the left inferior PV (LIPV) and left superior PV (LSPV) on the left side, and the right inferior PV (RIPV) and right superior PV (RSPV) on the right side (Fig. 1). A significant proportion (about 20%–30%) of the population have anatomical variations and the most common variations are extra right PVs (where, besides the RIPV and RSPV, one or more extra PVs emerge separately from the right side of the LA chamber) and the left common PV (where the LIPV and LSPV merge into one before joining the chamber). A personalized LA model can help to translate a generic ablation strategy to a patient's specific anatomy, thus making the ablation strategy more effective for this patient. Fusing the patient-specific LA model with electro-anatomical maps or overlaying the model onto 2-D real-time fluoroscopic images also provides valuable visual guidance during the intervention [Fig. 1(c)].

In this paper, we propose a fully automatic LA segmentation system on C-arm computed tomography (C-arm CT) data. Normally, a nonelectrocardiography-gated (i.e., non-ECG-gated or nongated) acquisition is performed for C-arm CT; therefore, it may contain cardiac motion artifacts, which blur thin boundaries between the LA and surrounding tissues. This presents a great challenge to nonmodel based segmentation approaches [5], [6], [9] (which assume no or little prior knowledge of the LA shape), although they may work well on highly-contrasted CT or magnetic resonance imaging (MRI) data. In our work, this challenge is addressed using a model based approach, which also takes advantage of a machine learning based object pose detector and boundary detector [10].

Instead of using one mean shape model as in [7], the PV anatomical variations are addressed using a part based model, where the whole LA is split into the chamber, appendage, four

Manuscript received August 09, 2013; revised September 05, 2013; accepted September 11, 2013. Date of publication October 04, 2013; date of current version January 30, 2014. *Asterisk indicates corresponding author.*

*Y. Zheng is with Imaging and Computer Vision Technology Field, Siemens Corporate Technology, Princeton, NJ 08540 USA (e-mail: yefeng.zheng@siemens.com).

D. Yang and D. Comaniciu are with Imaging and Computer Vision Technology Field, Siemens Corporate Technology, Princeton, NJ 08540 USA.

M. John is with Healthcare Sector, Siemens AG, 91301 Forchheim, Germany.

Digital Object Identifier 10.1109/TMI.2013.2284382

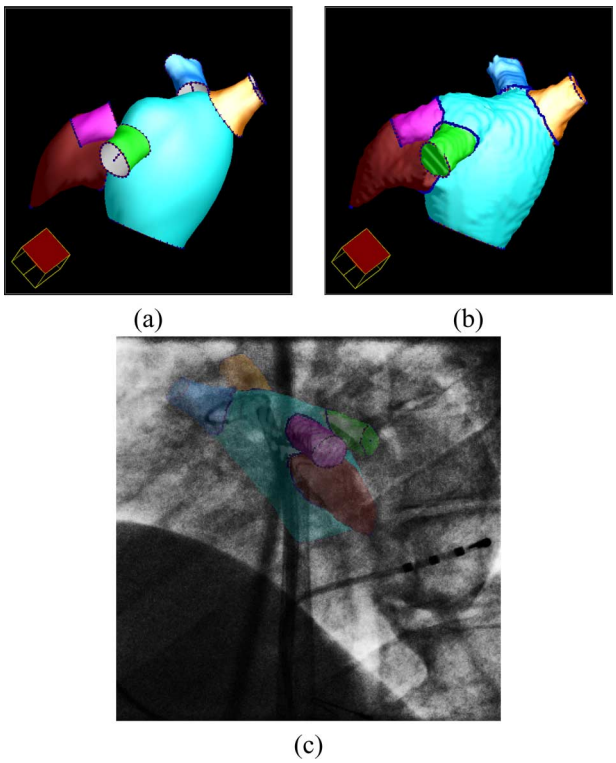

Fig. 1. The part based left atrium (LA) mesh model. (a) Meshes of the separate LA parts. (b) Final consolidated mesh model. (c) Overlay of the model onto a fluoroscopic image to provide visual guidance during catheter based ablation. Color scheme: Cyan for the LA chamber, dark red for the appendage, green for the left inferior pulmonary vein (PV), magenta for the left superior PV, orange for the right inferior PV, and blue for the right superior PV.

major PVs, and right middle PVs. Each part is a much simpler anatomical structure compared to the holistic one, therefore can be detected and segmented using a model based approach (except right middle PVs, which are segmented using a graph cuts algorithm). Statistical shape constraint is enforced during the detection of the PVs (estimating their pose parameters, including position, orientation, and size) to improve the robustness. After segmenting the LA parts, the gaps and overlaps among the parts are resolved and segmentation of the ostia region is further refined. As a common anatomical variation, extra right middle PVs are present in some patients. Depending on the presence or absence of right middle PVs, different ablation strategies or devices may be exploited by the physicians. Due to the large anatomical variations of right middle PVs, a purely model-based approach has difficulties to segment them [11]. In this work, a nonmodel-based graph cuts approach [12], [13] is exploited to segment the right middle PVs.

Please note, preliminary results of this work have been presented in our previous conference papers [14]–[16]. This paper revisits some components of the algorithm and presents more detailed description of the segmentation system. The remainder of this paper is organized as follows. In Section II, we present a brief review of the related work on LA segmentation. The part based LA model and the statistical shape constrained part detection/segmentation are presented in Section III. In Section IV, we present methods to refine the segmentation around the connections between different parts and determine the exact part boundary on the surface mesh. The graph cuts based right middle PV segmentation is described in Section V. Quantitative evaluation is performed in Section VI. In Section VII, we present a comparison with other methods followed by a discussion of the limitations of the proposed method. This papers concludes with Section VIII.

II. Related Work

Due to the complexity of the LA and PV anatomy, manual slice-by-slice segmentation may require 4–8 h per dataset depending on the number of slices to trace [17]. Various methods have been proposed to automate the segmentation procedure. The previous LA segmentation methods can be roughly categorized as nonmodel based and model based approaches. The nonmodel based approaches [5], [6], [9], [17]–[19] do not assume prior knowledge of the LA shape and the whole segmentation procedure is purely data driven. On the contrary, the model based approaches exploit a prior shape of the LA (either in the form of a mean shape mesh [7], [20]–[22] or an atlas [23], [24]) to guide the segmentation, therefore improving the segmentation robustness.

The nonmodel based approach proposed by John and Rahn [5] exploits the fact that the neighboring cardiac chambers can be separated by cuts at the narrowings of the blood pool. It relies on the assumption that the blood pool is highly contrasted, therefore can be extracted easily using a simple region growing method. This method has been adapted by Karim *et al.* [6], [25] to segment the LA in MRI angiographic images, where the blood pool is further enhanced by subtracting a noncontrasted volume from a contrasted one to remove bright bone tissues presented in both volumes. Cristoforetti *et al.* [18], [19] proposed a semi-automatic segmentation method where a user is required to put 20–30 markers on different cardiac anatomies and surrounding tissues. The marker controlled watershed algorithm is then applied to group unmarked voxels to the nearest markers. It takes 2–5 min to manually put markers and the segmentation procedure takes 21 min in addition. One advantage of nonmodel based methods is that they can handle anatomical variations of the PVs. However, such methods cannot provide the underlying anatomical information (e.g., which part of the segmentation is the left inferior PV). Anatomical information is beneficial to automatically warp an ablation strategy [26] (represented as planned ablation lines) onto the patient-specific anatomy. In practice, nonmodel based approaches work reasonably well on highly contrasted CT or MRI data, but they are not robust on challenging C-arm CT. Furthermore, some user interactions are often required to achieve satisfactory segmentation even on CT or MRI data [17].

The model based approaches exploit a prior shape of the LA to guide the segmentation. For example, Manzke *et al.* [7] built a mean shape of the combined structure of the LA chamber and four major PVs (right middle PVs are ignored) from a training set. With prior shape constraint, they could avoid the leakage around weak or missing boundaries, which plagues the nonmodel based approaches. Even after ignoring variable right middle PVs, it may still have difficulty to handle variations of left common PVs. Recently, this method has been extended to handle left common PVs and extra right PVs [11], [21], [22]. The PV variations are roughly categorized

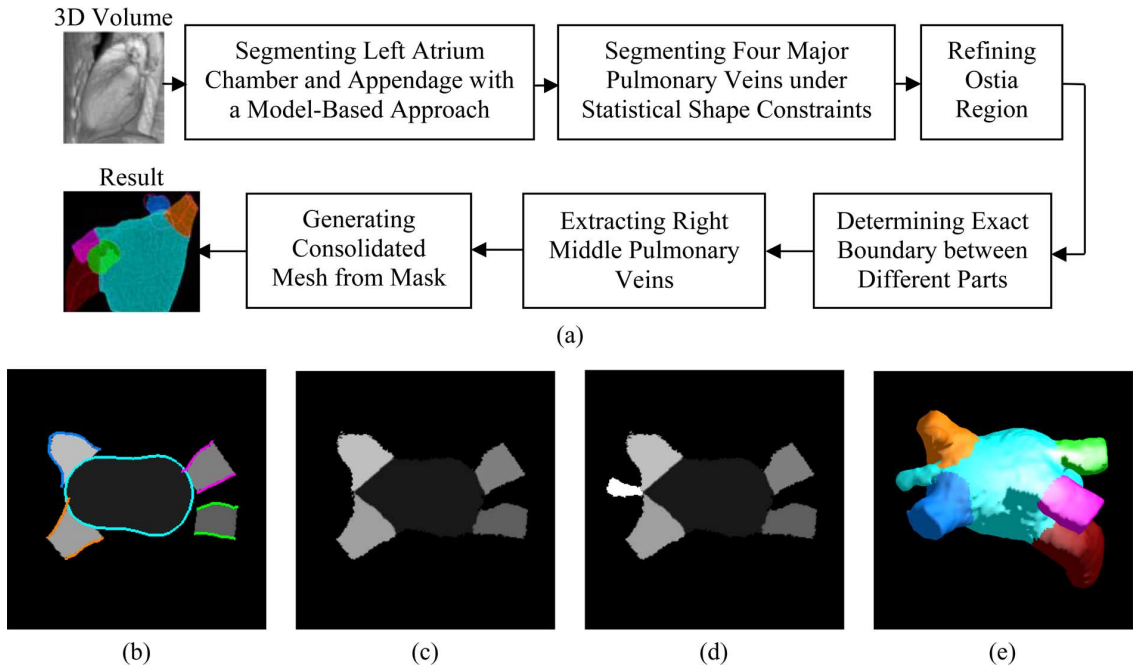

Fig. 2. Workflow of the proposed part based left atrium (LA) segmentation method and some intermediate results. (a) System diagram. (b) Mesh and mask after segmenting the LA parts. (c) Mask after resolving the gaps between parts and refining the ostia region. (d) Mask after extracting a right middle pulmonary vein. (e) Final consolidated mesh generated from the mask.

into a limited number of patterns [8]. During segmentation, the correct PV model needs to be automatically selected; otherwise, segmentation fails. However, automatic selection of a correct model incurs additional computing time. The methods have been tested on CT [21], [22] and MRI [11] data and a moderate success rate is achieved for the anatomical variation pattern identification. Furthermore, there are still a significant proportion of patients whose PV drainage patterns are not captured in the prebuilt shape models. The PV variations are addressed in [24], [27] using multiple atlases at the cost of extra computing time. Instead of summarizing the whole training set into average statistics, each training sample is treated as an atlas. The input volume is registered to each training sample and the corresponding labels are intelligently fused to get the segmentation result. The method is time consuming since each registration takes about 8 min and the overall segmentation time can easily go over 2 h with a handful of atlases.

Segmentation of the LA appendage has several applications in cardiac interventions. Occasionally, the ostium rim of the appendage is also ablated, especially for patients undergoing repeated catheter ablations [28]. More importantly, the ridge between the left superior PV and the appendage is a critical target to ablate. In addition, transcatheter LA appendage occlusion is an emerging minimally invasive technique to reduce the stroke risk for AF patients [29]. Explicit segmentation of the appendage is important for planning and visual guidance of this intervention. Previously, the appendage is often segmented implicitly in nonmodel based approaches [5]. We found only one work [30] explicitly segmenting the LA appendage using a deformable model. However, the deformable model has difficulty to reach the tip of the appendage and the segmentation completely fails on 1 out of 17 test datasets.

In this work, we exploit a part based LA model to handle anatomical variations. Part based models are popular in computer vision for object detection and recognition; however, its applications on medical image analysis are sparse. Toews and Arbel [31] applied a part based method for inter-subject brain MRI image registration. The parts are defined as salient regions, which do not correspond to a commonly-known anatomical structure. They further assume that the parts are conditionally independent once the pose of a reference anatomy is known. These are different to ours. Ecabert *et al.* [32] proposed to segment great vessels (including PVs) using an articulated model (a special part model). A vessel is composed of a few connected tubes, which are segmented sequentially from proximal to distal. An articulated model allows a larger deformation of the vessel than a holistic model; however, with a fixed topology, it lacks the flexibility to handle anatomical variations of the PVs.

III. Multi-Part Left Atrium Modeling and Segmentation

Our part based LA segmentation system is composed of multiple stages. Fig. 2 shows the workflow and some intermediate results during segmentation. In this section, we are focused on the modeling and segmentation of LA parts.

A. Part Based Left Atrium Model

As shown in Fig. 1(a), our part based LA model includes the LA chamber body, appendage, four major PVs, and optional right middle PVs (which are only present in some patients). We reuse the LA chamber model from our four-chamber heart model [10]. The LA chamber surface mesh is represented with 545 mesh points and 1056 triangles with an opening at the mitral valve. The mesh point correspondence is established using a rotation axis based resampling method. An interested reader is referred to [10] for more details.

For AF ablation, physicians only care about a short PV trunk connected to the LA chamber; therefore, we only detect a trunk

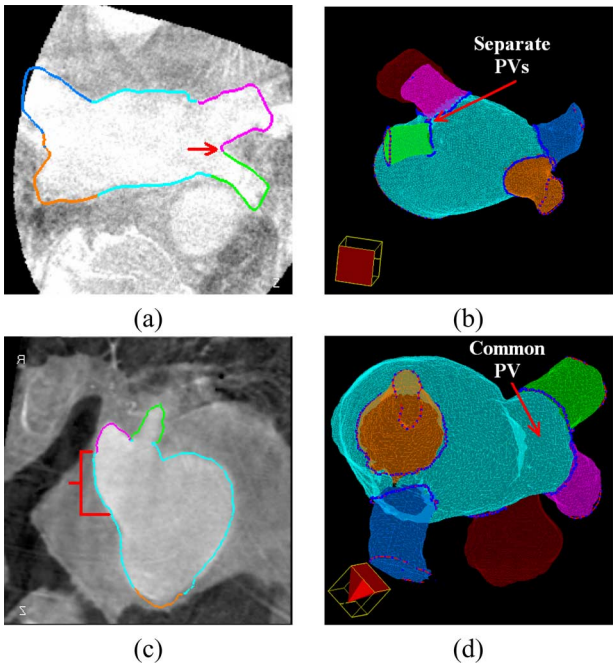

Fig. 3. Segmentation results on two datasets with different anatomical variations of the left pulmonary veins (PV). Images (a) and (b) show a patient with separate left inferior (green) and superior (magenta) PVs. Images (c) and (d) show a patient with a left common PV.

of 20 mm in length, originating from its ostium. In the case of a left common PV, the PVs after the bifurcation at the distal end of the common PV are modeled, as shown in Fig. 3(c) and (d). Each PV is represented as an open-ended tubular structure with a proximal opening on the LA chamber side and a distal opening away from the LA chamber. On the PV mesh, the two openings are represented as two closed contours, namely the proximal ring and the distal ring, respectively. The PV mesh is uniformly resampled to nine rings (including the proximal and distal rings) perpendicular to its centerline and each ring is uniformly resampled to 24 points; therefore, the PV mesh is represented by a total of 216 points and 384 triangles.

The LA appendage has a complicated shape, which is composed of a lot of small cavities. On C-arm CT, the boundary between cavities is often blurred due to the cardiac motion artifacts. In our application, it is accurate enough to use a smooth mesh tightly enclosing all the appendage cavities. The shape of the appendage mesh is close to a tilted cone with an opening (called a proximal ring) at the connection to the LA chamber. The centerline from the proximal ring center to the appendage tip defines the orientation of the tilted cone. Similar to the PVs, the appendage mesh is also represented as a set of uniformly distributed circular rings perpendicular to its centerline. Since the appendage is larger and has a more complicated shape than the PVs, it is represented as a denser mesh with 18 rings and each ring with 33 points. The most distal ring is represented as a single point to close the mesh at the appendage tip.

The right middle PVs are an optional component of our part based LA model as they are only present in a relatively small proportion of patients. Majority of the population (70%–80%) have no middle PVs. However, some patients may have up to three middle PVs [8]. The right middle PVs originate on the LA chamber around the area between two major right PVs. If the origin of a PV is too close to a major PV, it is often difficult to identify if this PV is an independent middle PV or just a side branch of a major PV. Due to these difficulties, we do not have a consistent mesh presentation of the right middle PVs. They are extracted using a nonmodel based graph cuts approach [12].

Please note, the part based LA model is an internal representation to facilitate the segmentation process in handling anatomical variations. The final LA model presented to physicians is a consolidated mesh with different parts labeled with different colors, as shown in Fig. 1(b).

B. Marginal Space Learning for 3-D Object Detection and Segmentation

Before diving into the details of the proposed LA segmentation approach, we briefly review the marginal space learning (MSL) based object detection/segmentation method [10], [33], which is the underlying technology for the segmentation of an LA part. MSL is an efficient and robust method for 3-D anatomical structure detection and segmentation in various medical imaging modalities. It is based on recent advances in learning discriminative models to exploit rich information embedded in a large expert-annotated database. We formulate the segmentation as a two-step learning problem: anatomical structure localization and boundary delineation.

Object localization (or detection) is a prerequisite for an automatic segmentation system and discriminative learning based approaches have proved to be efficient and robust for solving 2-D problems [34]. In these methods, object detection is formulated as a classification problem: whether an image block contains the target object or not. The object pose parameter space is quantized into a large set of discrete hypotheses and exhaustive search is used to pick the best hypothesis. To be specific, each hypothesis is tested by the trained classifier to get a detection score and the hypothesis with the largest score is taken as the final detection result. To accurately localize a 3-D object, nine pose parameters need to be estimated (three for translation, three for orientation, and three for anisotropic scaling). With the exponential increase of potential pose parameter combinations, exhaustive search is not practical for 3-D object detection. The idea of MSL is not to learn a classifier directly in the full similarity transformation space but to incrementally learn classifiers on marginal spaces. In our case, we split the estimation into three steps: position estimation, position-orientation estimation, and position-orientation-size estimation. After each step, we only keep a small number of promising hypotheses; therefore, the pose parameter space is pruned significantly to increase the detection efficiency.

After the MSL based pose estimation, we get the position, orientation, and size of the object. A mean shape is aligned to the estimated transformation to generate a rough estimate of the object shape. We then deform the shape to fit the object boundary using a machine learning based boundary detector within the active shape model (ASM) framework [35]. Interested readers are referred to [10], [33] for more details of the MSL based object detection and segmentation.

C. Constrained Detection of LA Parts

Our LA model contains multiple parts. The MSL based detection/segmentation works well for the LA chamber. However, independent detection of other parts is not robust, either due to low contrast (appendage) or a small object size (PVs). In C-arm CT, the appendage is particularly difficult to detect since it is a pouch without outlet and the blood flow is slow inside, preventing complete filling the appendage with contrast agent. In many datasets, the appendage is only barely visible. The MSL detector may pick the neighboring left superior PV (LSPV), which often touches the appendage and has higher contrast. However, the relative position of the appendage to the chamber is quite consistent. The comparison experiments presented in Section VI-C show that the best performance is achieved by treating the appendage and chamber as a consolidated object. One MSL based pose detector is trained to detect the combined object.

Through comparison experiments, we found neither a holistic approach nor independent detection worked for the PVs (refer to Section VI-C). In this paper, we propose to enforce statistical shape constraint [35] in PV detection. The point distribution model (PDM) is often used to enforce statistical shape constraint among a set of landmarks in the ASM. The shape variation is decomposed into orthogonal deformation modes through principal component analysis (PCA). A deformed shape is projected into a low dimensional deformation subspace to enforce statistical shape constraint. For each PV, an MSL pose detector can estimate nine pose parameters, i.e., three object center position parameters (T_x, T_y, T_z), three orientation Euler angles (O_x, O_y, O_z), and three anisotropic scaling parameters (S_x, S_y, S_z). Different to the conventional PDM, we also want to enforce constraint among the estimated orientation and size of PVs. One solution is to stack all PV pose parameters into a long vector to perform PCA. However, the position and orientation parameters are measured in different units. If not weighted properly, the extracted deformation modes may be dominated by one category of transformation. Furthermore, the Euler angles are periodic (with a period of 2π), which prevents the application of PCA.

In this work, we use a new presentation of the pose parameters to avoid the above problems. The object pose can be fully represented by the object center $T = (T_x, T_y, T_z)$ together with three scaled orthogonal axes. Alternative to the Euler angles, the object orientation can be represented as a rotation matrix $R = [R_x, R_y, R_z]$ and each column of R defines an axis. The object pose parameters can be fully represented by a four-point set (T, V_x, V_y, V_z), where

$$V_x = T + S_x R_x, \quad V_y = T + S_y R_y, \quad V_z = T + S_z R_z. \quad (1)$$

The pose of each PV is represented as four points. Besides the constraint among the PVs, we also add the already detected LA chamber center and appendage center to stabilize the detection. In total, we get a set of 18 points and a shape space is learned on a training set.

After independent detection of the center, orientation, and size of the PVs, we project their poses into a subspace with eight dimensions (which explains about 75% of the total variation) to enforce statistical shape constraint. After that, we get a new four-point set $(\hat{T}, \hat{V}_x, \hat{V}_y, \hat{V}_z)$ for each PV. We then recover the orientation $(\hat{R})$ and scale $(\hat{S})$ by inversion of (1) as $\hat{S}_i = \|\hat{V}_i - \hat{T}\|$ and $\hat{R}_i = (\hat{V}_i - \hat{T})/\hat{S}_i$ for i being x, y, z in turn. However, the estimate $\hat{R} = [\hat{R}_x, \hat{R}_y, \hat{R}_z]$ is generally not a true rotation matrix $(\hat{R}^T\hat{R} \neq I)$. We want to find the nearest rotation matrix R_o to minimize the sum of squares of elements in the difference matrix $R_o - \hat{R}$, which is equivalent to

$$R_o = \arg\min_{\mathrm{R}} \mathrm{Trace}((R - \hat{R})^T(R - \hat{R})) \quad (2)$$

subject to $R_o^T R_o = I$. Here, $\mathrm{Trace}(.)$ is a sum of the diagonal elements. The optimal solution [36] is given by

$$R_o = \hat{R}(\hat{R}^T\hat{R})^{-1/2}. \quad (3)$$

By enforcing statistical shape constraint, a proper configuration of the different LA parts is preserved. On C-arm CT acquired with a small X-ray detector panel, a PV may be partially outside of the field-of-view. Using the proposed method, such a PV can still be detected correctly [e.g., the RSPV (blue) in Fig. 3(a)]. After pose estimation, the detailed boundary of a PV is segmented using a machine learning based boundary detector within the ASM framework [10].

IV. Precise Segmentation of Ostia Region of Pulmonary Veins and Appendage

In this section, we first discuss how to convert the separate part meshes to a mask to eliminate the gaps and intersections among parts (Section IV-A). In Sections IV-B and IV-C, we then present methods for precise segmentation of the ostia region of the pulmonary veins and appendage, which are main ablation focus. At last, a scheme for proper part labeling is proposed in Section IV-D to determine the exact boundary between different LA parts.

A. Mesh to Mask Conversion

After constrained detection and segmentation, we get six separate meshes (the LA chamber, appendage, and four PVs), as shown in Fig. 4(a). There may be gaps and/or intersections among different meshes. Physicians prefer a consolidated mesh with different anatomical structures labeled with different colors. We first project the proximal ring of a PV or appendage along the centerline onto the LA chamber to eliminate the gaps among different mesh parts [Fig. 4(b)]. Now, the part meshes are fully connected. However, the mesh intersections of different parts may still exist. It is complicated to work directly on the meshes. Instead, we convert the meshes to a volume mask [Fig. 4(c)], and a new mesh [Fig. 4(d)] can be generated from the volume mask using the marching cubes algorithm [37]. Since pure mesh operation is performed to connect PV/appendage meshes to the LA chamber, the ostia region is not segmented accurately and needs to be further refined using the approaches detailed in the following.

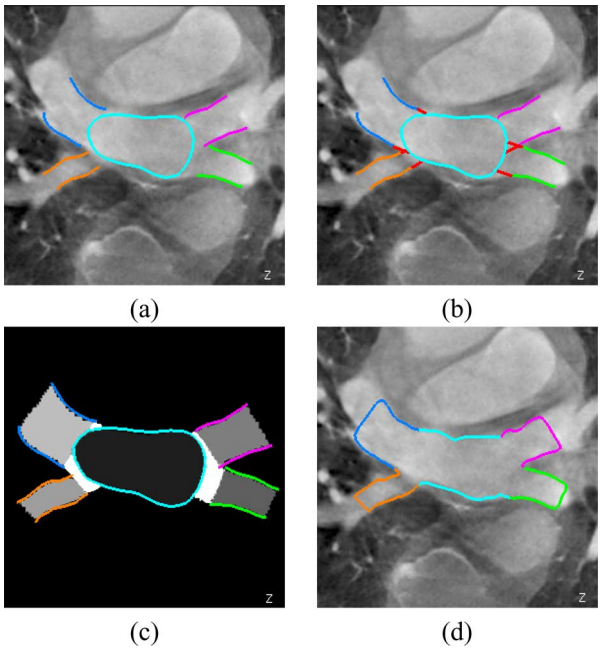

Fig. 4. Generating a consolidated left atrium (LA) mesh from separate parts. (a) Separate meshes of the pulmonary veins (PV) and LA chamber. (b) After connecting the PV meshes to the LA chamber. The added mesh pieces are shown in red. (c) Volume mask generated from the meshes. (d) Consolidated mesh.

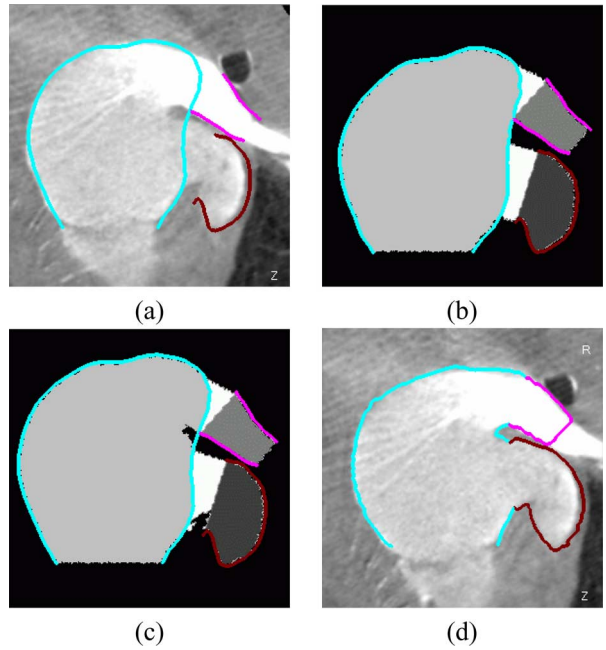

Fig. 5. Refinement of the segmentation of the ridge between the left superior pulmonary vein (LSPV) and appendage. (a) An intersection of a volume overlaid with the LA part meshes with cyan for the chamber, dark red for the appendage, and magenta for the LSPV. (b) Mask after connecting the PV/appendage meshes to the chamber. The initial ostia region is shown in white. (c) Mask after erosion to remove dark voxels from the mask. (d) Final consolidated mesh.

B. LSPV-Appendage Ridge Refinement

Sometimes, the ridge between the LSPV and the appendage is not delineated accurately, especially when the LSPV and the appendage are close to each other. As shown in Fig. 5(a), a narrow ridge is partially enclosed inside the LA chamber mesh. To refine the segmentation around the ridge, we perform layer-by-layer erosion to remove dark voxels. We first find the outer layer of the chamber and ostia regions. (Please note the mask of the PVs and appendage is excluded from erosion since the model-based segmentation normally gives accurate and satisfactory segmentation.) If a voxel on the outer layer has an intensity less than a threshold, we set it to a background voxel. Such layer-by-layer erosion is performed 10 iterations. This erosion operation not only improves the segmentation of the ridge, but also other regions. For example, as shown in Fig. 5(c), the dark voxels in the ostia region between the appendage and the chamber are removed, resulting in more accurate segmentation around that region too. C-arm CT normally has a high intensity variation due to the lack of a standard protocol for the use of contrast agent. A fixed erosion threshold does not work for all datasets. Instead, we automatically determine an adaptive threshold for each dataset based on the analysis of the ostia region intensity. To be specific, we sort the intensity of the ostia region and use the lower 2.5th percentile as the erosion threshold. Experiments show that this parameter setting results in satisfactory segmentation.

C. Ostia Region Refinement

The initial ostia region is labeled with pure mesh operation by projecting the PV/appendage meshes onto the chamber. The segmentation is often not accurate enough when the part gap

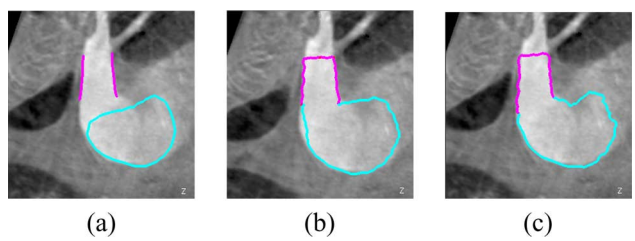

Fig. 6. Segmentation of the ostia region of the left superior pulmonary vein. (a) Separate meshes. (b) Consolidated mesh without refinement. (c) Consolidated mesh after refinement.

is too large [see Fig. 6(b)]. We perform layer-by-layer region growing to refine the segmentation using an adaptive threshold (i.e., the 50th percentile of the initial ostia region intensity). Region growing may leak into neighboring highly contrasted structures, e.g., the descending aorta that is close to the LIPV, due to the missing image boundary under cardiac motion artifacts. On rare cases, it may leak into interventional devices (e.g., the transesophageal echocardiographic (TEE) probe in Fig. 7). As a less severe problem, the resulting boundary after region growing are often quite zig-zag due to the imaging noise.

To fix these issues, we fit a smooth mesh in the ostia region (as shown in Fig. 8). The mesh is initialized as a tube, which is generated as follows. We first extend the proximal ring of a PV (or appendage) into the chamber, and then triangulate the surface between the original proximal ring and the extended ring as an initial mesh. Each mesh point is moved along the surface normal to the first transition from a masked voxel to background. Many leaked voxels are already excluded from the adjusted mesh.

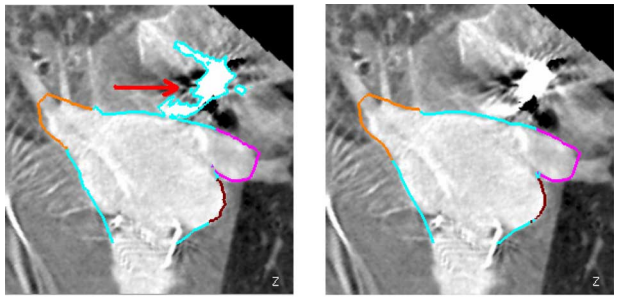

(a) (b)

Fig. 7. Avoid segmentation leakage. (a) After region growing, the segmentation leaks into the neighboring ultrasound probe. (b) Segmentation result after enforcing smoothness of the ostia region.

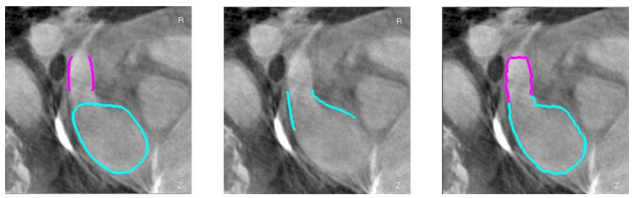

(a) (b) (c)

Fig. 8. Fitting an optimal smooth mesh to the left superior pulmonary vein (LSPV) ostia region. (a) Separate part meshes (cyan for the chamber and magenta for the LSPV). (b) Fitting a smooth mesh onto the ostia region. (c) Final mesh.

However, the resulting mesh is not smooth and it may still include leakage. Finally, we search for an optimal smooth mesh by shrinking mesh points along the surface normal.

A triangulated surface can be represented as a graph $S = \{V, E\}$, where V is an array of vertices and E is an array of edges. For each vertex V_i on the surface, we can define a neighborhood $\mathcal{N}_i$. Normally, first order neighborhood is used that vertex j is a neighbor of vertex i if they are connected by an edge. The smoothness around a vertex is often defined as [38]

$$\nabla V_i = \sum_{j \in \mathcal{N}_i} \frac{1}{\#\mathcal{N}_i}(V_j - V_i) \tag{4}$$

where $\#N_i$ is the number of neighbors for vertex i. The smoothness of the whole surface is

$$SM(S) = \sum_i \|\nabla V_i\|^2. \tag{5}$$

We want to adjust the mesh to generate a smooth surface by minimizing (5). Since there is too much freedom to adjust a mesh, similar to the well accepted practice in active contours [39] and the ASM [35], we only allow the adjustment along the normal direction

$$V_i' = V_i + \delta_i N_i \tag{6}$$

where δ_i is a scalar and N_i is the surface normal at vertex i. We can further limit the adjustment of each vertex by enforcing the following constraints:

$$l_i \leq \delta_i \leq u_i \tag{7}$$

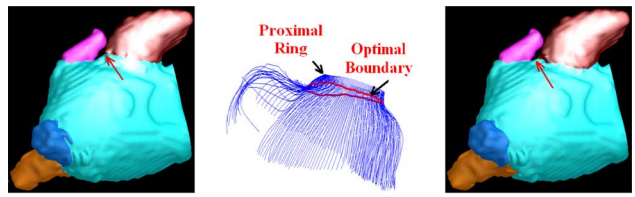

(a) (b) (c)

Fig. 9. Refine the mesh part label. (a) Before label refinement. (b) Optimal boundary (the red contour) between the left atrial appendage and the chamber. (b) After label refinement.

where l_i and u_i are the lower and upper bound of the adjustment for vertex i, respectively. For example, in this application, we enforce $\delta_i \leq 0$ to guarantee that the mesh is completely embedded inside the masked ostia region. (Note, the surface normal is pointing outside of the mesh.)

In practice, we also need to get a trade-off between smoothness and the amount of adjustment. Our final optimization problem is

$$\min F = \sum_i \left\| \sum_{j \in \mathcal{N}_i} \frac{1}{\#\mathcal{N}_i}(V_j' - V_i') \right\|^2 + \alpha \sum_i {\delta_i}^2 \tag{8}$$

subject to the bound constrain of $\delta_i \leq 0$. Here, $\alpha \geq 0$ ($\alpha = 0.06$ throughout the experiments) is a scalar for the above trade-off.

It turns out that our optimization problem is a classical quadratic programming problem. For $\alpha > 0$, the objective function defined in (8) is a strictly convex function; therefore, it has a unique global optimal solution, which is solved using the algorithm proposed in [40].

Fig. 8(b) shows the optimal smooth mesh fitting around the LSPV ostia region. A smooth mesh is fit in each ostia region (in total of five) and an ostia region voxel is included in the final mask if it is inside at least one ostia mesh. After fitting an optimal smooth mesh around the ostia region, we can achieve a smooth mesh in the final segmentation and at the same time prevent leakage [as shown in Fig. 7(b)].

D. Mesh Part Labeling

Using the above techniques, the ostia regions of the PVs and appendage are segmented. However, the boundary between the different LA parts is often not labeled correctly, resulting in wrong colors for some mesh triangles, as shown in Fig. 9(a). In this section, we present an optimization based approach to refining the final mesh part labeling.

Normally, the boundary between different parts has high surface curvatures on the mesh. However, sometimes, the connection can be smooth; therefore, the exact boundary around those regions need to be extrapolated by the neighboring regions with high curvatures. We propose an optimization based approach to searching for the part boundary. First, the proximal ring of a PV (or the appendage) is densely resampled to a fine resolution (e.g., 0.25 mm). Suppose the proximal ring center is C. Given a proximal ring point P_i, a plane is determined that is perpendicular to the proximal ring plane, and passes P_i and C. Starting from point P_i, we trace the mask boundary (the boundary between foreground voxels and the background) on the plane. The

tracing stops if it encounters a masked voxel of another PV (or the appendage) or the maximum length is traced (e.g., 60 mm). The traced contour is then uniformly resampled to a high resolution (e.g., 0.25 mm). Fig. 9(b) shows the traced contours from the appendage proximal ring. This procedure generates a set of points Q_i^j. Here, Q_i^j indicates the jth point on the ith contour and $Q_i^0 = P_i$.

We then search for a smooth part boundary B with the maximum sum of curvatures

$$B = \left(Q_0^{J(0)}, \ldots, Q_{n-1}^{J(n-1)}\right) = \underset{J(0),\ldots,J(n-1)}{\arg\max} \sum_{i=0}^{n-1} C\left(Q_i^{J(i)}\right). \quad (9)$$

Here, $C(Q_i^j)$ is the curvature at point Q_i^j, which is defined as [41]

$$C\left(Q_i^j\right) = \left\|\left(Q_i^{j+1} - Q_i^j\right) - \left(Q_i^j - Q_i^{j-1}\right)\right\| = \left\|2Q_i^j - Q_i^{j-1} - Q_i^{j+1}\right\|. \quad (10)$$

As a second-order derivative of a contour, curvature estimation is error prone; therefore, for some datasets, the final part boundary B may be stuck in a position a bit away from the chamber. To achieve a more robust result, we add a small amount of bias, $\|N \cdot (Q_i^j - Q_i^0)\|$, in the cost function to push the part boundary toward the chamber. Here, N is the normal of the proximal ring and $\|N \cdot (Q_i^j - Q_i^0)\|$ is the magnitude of the dot-product between vectors N and $Q_i^j - Q_i^0$, therefore measuring the perpendicular distance from Q_i^j to the proximal ring plane. We enforce the smoothness of the part boundary by constraining the distance of neighboring $Q_i^{J(i)}$ and $Q_{i+1}^{J(i+1)}$ to

$$\|J(i) - J(i+1)\| \leq 1. \quad (11)$$

The part boundary should form a closed contour, therefore

$$\|J(n-1) - J(0)\| \leq 1. \quad (12)$$

The final optimization problem is formalized as

$$B = \underset{J(0),\ldots,J(n-1)}{\arg\max} \sum_{i=0}^{n-1} C\left(Q_i^{J(i)}\right) + w\left\|N \cdot \left(Q_i^{J(i)} - Q_i^0\right)\right\| \quad (13)$$

subject to smoothness constraints of (11) and (12). Here, w is a weight adjusting the bias toward a boundary close to the chamber. Throughout our experiments, we set $w = 0.001$. The optimal part boundary can be solved efficiently using a dynamic programming algorithm to achieve a global optimal solution.

Fig. 9 shows the mesh before and after part label refinement. The appendage mesh is successfully extended toward the chamber in this example.

V. Right Middle Pulmonary Vein Segmentation

Due to the anatomical variations, it is difficult to use a model based approach to segmenting the right middle PVs. In this work, we exploit a nonmodel based graph cuts approach [12] to extracting the right middle PVs. Nongated C-arm CT may contain severe motion artifacts; therefore, a graph cuts approach tends to leak to other tissues if the segmentation is not constrained. Here, the already segmented LA parts (the LA chamber, RIPV, and RSPV) are used to constrain the segmentation since the right middle PVs originate on the LA chamber surface inside the area between two major right PVs. For this purpose, a region-of-interest (ROI) is generated automatically, as shown in Fig. 10, with the centerlines of the RIPV and RSPV serving as the boundary of the ROI.

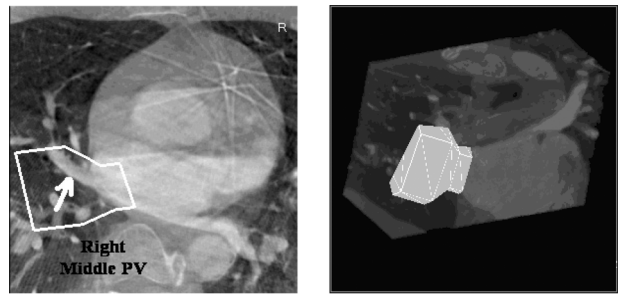

(a) (b)

Fig. 10. Region of interest (ROI) for the right middle pulmonary vein extraction. (a) ROI overlaid on trans-axial slice of a C-arm CT volume. (b) ROI mesh embedded in a 3-D visualization of the data.

The performance of graph cuts is dominated by the initial positive (the LA parts) and negative (background) seeds. Naturally, the positive seeds are set as those voxels inside the ROI that are already segmented as part of the LA, RIPV, or RSPV. Since the background is normally darker than the contrasted PVs, the negative seeds are selected from the dark voxels inside the ROI. A certain percentage ζ of the darkest voxels are almost sure to belong to the background; therefore, they are set as negative seeds. Parameters ζ is critical in determining the accuracy of the final segmentation. With a small ζ (which results in a small number of negative seeds), we can detect the right middle PVs with low contrast, but leakage may occur. With a large ζ, we can avoid leakage, but some dark right middle PVs would be misdetected. In this work, we choose a relatively small ζ (lower 85th percentile of the voxel intensities inside the ROI) to achieve a high detection rate. Leakage (false positive PVs) is then removed in a postprocessing step.

After setting the positive and negative seed points, a graph is built for all voxels inside the ROI [12]. Neighboring voxels (six-connected neighborhood) form edges in the graph and the edge weight ω is set as

$$\omega = \exp\left[-\frac{(I_p - I_q)^2}{2\sigma^2}\right]. \quad (14)$$

Here, $I_{p,q}$ are the intensities of neighboring voxels p and q, and σ is the standard deviation of intensity distribution of the ROI. The optimal label assignment (foreground or background) of all voxels inside the ROI can be solved with the efficient min-cut/max-flow algorithms. Please refer to [12] and [42] for more details of the graph cuts based segmentation algorithm.

As mentioned before, to achieve a high detection rate, we intensionally use a relative small threshold ζ for setting background seeds. Mild leakage may happen on some data and a

pruning procedure is then exploited to remove false positive detections based on multiple criteria. We first perform connected component analysis for the newly detected foreground voxels. Isolated components not connected to any existing LA part are eliminated as noise. The remaining connected components, CCs, are labeled as the LA chamber, RIPV or RSPV according to the label of the part they are connected to. After that, multiple criteria are adopted to determine if a CC is a false positive or not.

First, we check the location where a CC touches other LA parts (i.e., chamber, RIPV, and RSPV) because the right middle PVs should originate from the LA chamber surface, not from a distal end of a major PV trunk. Therefore, a CC is regarded as a false positive and removed if it touches the distal end of the RIPV or RSPV trunk.

Second, we check if the shape of a CC is close to a tube based on principal component analysis (PCA). For a tubular-shaped PV, the length along the major axis would be much larger than the lengths along the other two axes. We calculate the co-variance matrix of the position of all voxels belonging to the CC and the PCA eigenvalues $\lambda_{i=0,1,2}(\lambda_0 \geq \lambda_1 \geq \lambda_2 > 0)$ of the co-variance matrix represent the lengths along three orthogonal axes. Thus, a CC is regarded as a true PV if $\lambda_0 \gg \lambda_1$ and $\lambda_1 \approx \lambda_2$. In our experiment, the criteria are set as $\lambda_0 > 3\lambda_1$ and $2\lambda_2 > \lambda_1 > \lambda_2$.

At last, for a tubular-shaped CC, we check its maximum radius $R_{\max}(\mathrm{CC})$. For each voxel p in a CC, we calculate the minimum distance $D_{\min}(p)$ to a background (bg) voxel

$$D_{\min}(p) = \min_{\forall q \in bg} \sqrt{(p_x - q_x)^2 + (p_y - q_y)^2 + (p_z - q_z)^2}. \tag{15}$$

The maximum radius of a CC is defined as

$$R_{\max}(\mathrm{CC}) = \max_{p \in \mathrm{CC}} D_{\min}(p). \tag{16}$$

Normally, a right middle PV is much slimmer than the RIPV and RSPV; therefore a CC is a false positive if its maximum radius $R_{\max}$ is larger than a threshold $R_{\mathrm{threshold}}$ ($R_{\mathrm{threshold}} = 4$ mm throughout the experiments).

VI. Experiments

A. Data Sets

We collected 687 C-arm CT datasets, scanned by Siemens Axiom Artis zee C-arm systems at 18 clinical sites in Europe and the USA from June 2006 to April 2011. Among them 253 datasets were scanned with large X-ray detector panels (30×40 cm^2) and were reconstructed to volumes composed of 85–254 slices (each slice containing 256×256 pixels). The resolution varies from 0.61 mm to 1.00 mm. A typical large volume has $256 \times 256 \times 190$ voxels with an isotropic resolution of 0.90 mm. The other 434 datasets were scanned with small X-ray detectors (20×20 cm^2). Each volume contains 164–251 slices and each slice has 256×256 pixels. The resolution also varies. A typical small volume has $256 \times 256 \times 245$ voxels with an isotropic resolution of 0.44 mm. Because of the limited field-of-view of small X-ray detectors, the reconstructed volumes may contain artifacts, especially around the volume margin.

Contrast agent (about 80–100 ml) is injected via a pigtail catheter inside the pulmonary artery trunk. A single sweep of the C-arm (a rotation of 200° in 5 s) is performed to capture 2-D projections and a 3-D volume is reconstructed from all 2-D projections belonging to various cardiac phases (the so-called nongated reconstruction). Such nongated acquisition often results in significant amount of motion blur, especially around the septum wall of the LA. In most cases, the LA has sufficient contrast, but inhomogeneous contrast filling is often observed (Fig. 5), especially between the left and right PVs because of the different transition time of the contrast agent from the pulmonary artery trunk to the PVs. The LA appendage often lacks contrast because of the slow blood flow inside the appendage. Different to [7], [43], our imaging protocol uses a single scan to reduce the amount of contrast agent and radiation dose, even for a C-arm system with a small X-ray detector.

B. Ground Truth

The LA parts (including LA chamber, appendage, and four major PVs) are annotated using the part model presented in Section III-A, which are then used to train the part detectors (Section III-C). The mesh point correspondence is established using mesh resampling methods, as described in Section III-A. A part based annotation is sufficient to train the system since the other LA segmentation components, including the creation of a consolidated mesh from part based segmentation (as described in Section IV) and extraction of right middle PVs (as described in Section V), do not use a machine learning based technology.

Since the final LA segmentation presented to physicians is a consolidated mesh, as shown in Fig. 1(b), to evaluate the overall segmentation accuracy, we also create another annotation using the consolidated mesh. Starting from a part based annotation, a consolidated mesh is generated using the methods presented in Section IV. The mesh is then double checked and segmentation errors are manually corrected. The following evaluation of segmentation accuracy is against the consolidated mesh annotation. The consolidated mesh is not used for training and no mesh point correspondence is required.

The right middle PVs are much more difficult to annotate since they are thin and have variable shapes. On some datasets, they may be confused with a side branch of a major PV if the origin of the side branch is close to the ostium of a major PV. Instead of using a mesh annotation, the right middle PVs are annotated at the voxel level. A paint brush tool is developed to paint all voxels inside the ROI (Fig. 10) as foreground or background. Therefore, not only the right middle PVs are painted; the lowly-bifurcated side branches are also painted as long as they are inside the ROI. The voxel-wise annotation is performed slice-by-slice. Due to the difficulty of the annotation process, the right middle PVs are annotated only on a subset of the data. We randomly select 70 cases from the large X-ray detector data and 70 cases from the small data, resulting in a total of 140 annotated cases. A total of 88 right middle PVs are identified from these

TABLE I
LEFT ATRIUM SEGMENTATION ERRORS (BASED ON FOUR-FOLD CROSS-VALIDATION) ON 253 LARGE C-ARM CT VOLUMES. SYMMETRIC SURFACE-TO-SURFACE ERRORS, MEASURED IN MILLIMETERS (MM), ARE REPORTED

	Holistic				Independent				Proposed			
	Mean	Std	Median	Max	Mean	Std	Median	Max	Mean	Std	Median	Max
LA Chamber	1.52	0.69	1.38	12.86	1.45	0.71	1.26	12.83	**1.39**	0.66	1.22	11.76
Appendage	3.16	2.80	2.51	14.81	3.39	3.87	2.52	15.05	**2.80**	2.76	2.13	14.11
Left Inf. PV	2.68	1.92	2.10	9.89	1.67	1.36	1.32	7.88	**1.58**	1.12	1.27	7.49
Left Sup. PV	2.45	2.10	1.74	9.42	1.72	1.36	1.38	8.40	**1.53**	1.12	1.15	7.54
Right Inf. PV	3.24	2.52	2.39	11.33	1.85	2.64	1.30	7.79	**1.63**	1.45	1.33	7.55
Right Sup. PV	2.31	1.53	1.86	9.35	1.42	1.31	1.15	6.69	**1.32**	0.71	1.20	6.58
Whole Mesh Average	2.08	0.85	1.94	11.86	1.85	1.00	1.59	11.30	**1.65**	0.75	1.48	10.45
Whole Mesh (No Part Label)	1.72	0.60	1.61	10.57	1.51	0.63	1.37	9.94	**1.42**	0.54	1.29	9.45
Whole Mesh (No Part Label + No LAA)	1.55	0.57	1.45	10.30	1.30	0.54	1.15	9.61	**1.25**	0.49	1.11	9.07

TABLE II
LEFT ATRIUM SEGMENTATION ERRORS (BASED ON A FOUR-FOLD CROSS-VALIDATION) ON 434 SMALL C-ARM CT VOLUMES. SYMMETRIC SURFACE-TO-SURFACE ERRORS, MEASURED IN MILLIMETERS (MM), ARE REPORTED

	Holistic				Independent				Proposed			
	Mean	Std	Median	Max	Mean	Std	Median	Max	Mean	Std	Median	Max
LA Chamber	1.45	0.74	1.26	13.31	1.42	0.74	1.22	13.74	**1.34**	0.61	1.16	12.61
Appendage	2.41	1.68	1.98	12.20	3.11	2.96	2.32	14.42	**2.40**	1.60	1.95	12.72
Left Inf. PV	2.71	2.48	1.97	10.02	1.94	2.70	1.22	8.16	**1.66**	1.66	1.18	7.72
Left Sup. PV	2.73	2.76	1.72	9.93	2.23	2.76	1.33	9.43	**1.60**	1.72	1.03	7.74
Right Inf. PV	2.80	2.10	2.19	10.51	1.83	3.25	1.30	7.94	**1.58**	1.30	1.31	7.42
Right Sup. PV	2.21	1.70	1.71	9.30	1.63	2.60	1.07	7.36	**1.36**	1.21	1.05	6.68
Whole Mesh Average	1.90	0.89	1.68	11.78	1.84	1.12	1.56	11.82	**1.57**	0.70	1.39	10.79
Whole Mesh (No Part Label)	1.60	0.65	1.45	10.75	1.47	0.77	1.29	10.34	**1.35**	0.54	1.22	9.88
Whole Mesh (No Part Label + No LAA)	1.51	0.66	1.36	10.88	1.31	0.73	1.14	10.30	**1.23**	0.53	1.09	9.85

140 patients. Among them, 63 patients have no middle PVs; 67 have one middle PV; nine have two middle PVs; and one patient has three middle PVs.

C. Evaluation of LA Segmentation

A four-fold cross-validation is performed to evaluate the LA segmentation accuracy. The whole dataset is randomly split into four roughly equal sets. Three sets are used to train the system and the remaining set is reserved for testing. The configuration is rotated, until each set has been tested once. Due to the heterogeneity of the datasets, we train two separate systems for the large and small volumes, respectively. The evaluation is performed separately for different data categories.

The LA segmentation accuracy (excluding the right middle PVs) is measured using the symmetric surface-to-surface distance [10]. For each point on a mesh, we search for the closest point on the other mesh to calculate the minimum distance. Different anatomical parts are labeled differently on our consolidated mesh. To include the mesh part labeling errors in the evaluation, when we search for the closest corresponding point, the search is constrained to the region with the same part label. The minimum distances of all mesh points are averaged to calculate the mesh-level error. We calculate the distance from the detected mesh to the ground-truth and vice versa to make the measurement symmetric. The mean, standard deviation, and median of the mesh-level errors over the whole dataset are reported in Tables I and II. The maximum errors are also reported, which are calculated differently as follows. For each detected mesh point, the minimum distance to the ground truth is calculated as previously. We then search for the largest error over the whole mesh. The maximum error is also calculated from the ground truth to the detected mesh and the larger value of these two errors is recorded as the maximum error for the volume. The average of the maximum errors over the whole dataset (with multiple volumes) is reported in Tables I and II. Our consolidated mesh has an opening around the mitral valve so that the physicians can have an endocardium view inside the LA. The mesh is closed around the distal PVs although there is no image boundary around that region. Similar to [7], the artificial closings around the distal PVs are excluded from the evaluation (which corresponds to about 5.5% mesh triangles excluded). Please note, the segmentation errors reported in our previous work [14], [15] include the artificial closings, resulting in slightly larger errors.

Tables I and II show segmentation errors of the consolidated mesh using various approaches on the large and small volumes, respectively. The comparison is limited to the variations in the LA part detection. After that, we use the same procedure for boundary delineation and consolidated mesh generation. The break-down errors of the LA parts are shown separately and the row "*Whole Mesh Average*" shows the average errors of the whole mesh. If we treat the whole LA as a holistic object, the segmentation errors are large, especially for the PVs due to the anatomical variations. Independent detection of the parts can improve the PV segmentation accuracy. However, the LA appendage segmentation is deteriorated. Using the proposed method, we achieve consistent improvement for all LA parts on both the large and small volumes. On average, we achieve an error of 1.65 mm for the large volumes, which corresponding to

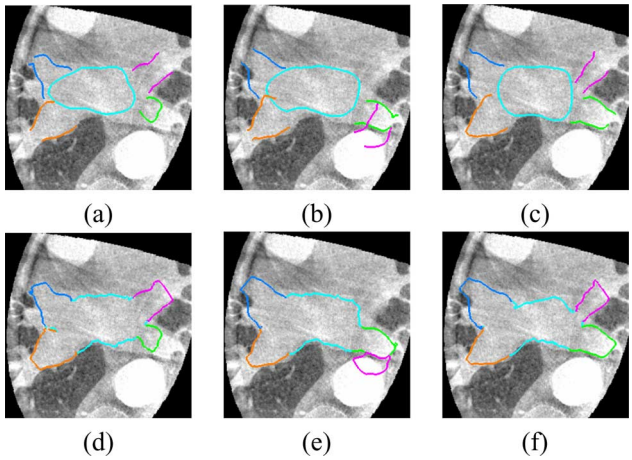

Fig. 11. Left atrium segmentation results on a small volume using different part detection methods. The top row shows part detection results and the bottom row shows final consolidated meshes. (a) and (d) Holistic detection. (b) and (e) Independent detection. Due to low contrast in the heart, the descending aorta is detected as the left superior pulmonary vein (magenta). (c) and (f) The proposed method.

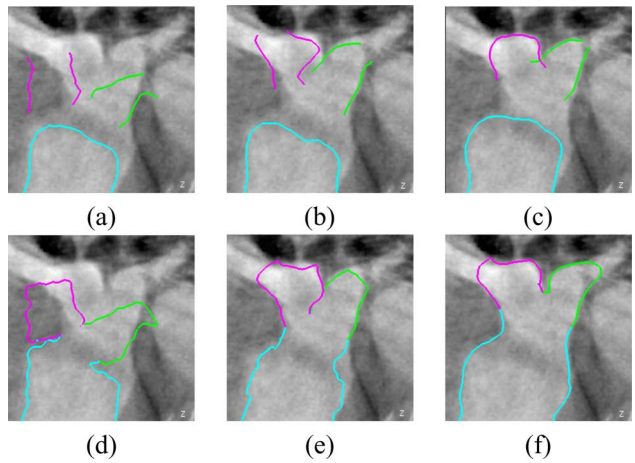

Fig. 12. Left atrium segmentation results on a large volume using different part detection methods. The top row shows part detection results and the bottom row shows final consolidated meshes. (a) and (d) Holistic detection. This patient has a left common pulmonary vein, which cannot be handled with a single holistic model. (b) and (e) Independent detection. (c) and (f) The proposed method.

26% reduction compared to the holistic approach and 12% reduction to the independent detection. A slightly smaller average error of 1.57 mm is achieved for the small volumes, partially due to the higher voxel resolution and higher contrast inside the LA. In addition, we have more small volumes for training and cross-validation (434 versus 253). This error corresponds to 17% reduction to the holistic approach and 15% reduction to the independent detection. In our approach, the inferior PVs have larger errors than the superior PVs since they are more likely to be cut by the volume borders.

Fig. 11 shows LA segmentation results on a small volume using different part detection methods. Due to low contrast in the heart, independent detection picks the descending aorta as the LSPV (magenta). By enforcing statistical shape constraint during the detection of PVs, the LSPV is detected correctly. Fig. 12 shows another example from a patient with a left common PV. The holistic LA model cannot handle such an anatomical variation, therefore fails to detect the LIPV and LSPV. Using the proposed part based LA model, the anatomical variation can be handled elegantly.

D. Evaluation of Right Middle PV Extraction

The segmentation accuracy of the right middle PVs is also evaluated using the surface-to-surface errors by converting the voxel-wise annotation to a mesh using the marching cubes algorithm [37]. The errors of the mesh inside the ROI of right middle PVs are calculated. The mean mesh error is 1.32 mm for the large volumes and 1.07 mm for the small volumes (as shown in Table III).

The mesh errors do not provide semantic meaning of the segmentation (e.g., the number of misdetected middle PVs); therefore, we also evaluate the vessel-wise errors. In total, there are 49 right middle PVs in the 70 large volumes. The proposed method detects 43 of them (87.8%). The misdetections are mainly caused by small PVs with insufficient contrast. A similar vessel-wise detection rate is achieved for the small X-ray panel data. The false positive rate is quite low. In total, there are only three and five false positive PVs detected over the whole dataset of large and small volumes, respectively. The false positives are mainly due to the *ghost* vessels generated by the motion artifacts. Fig. 13 shows an example of an extracted right middle PV.

VII. Discussions

A. Comparison With Previous Methods

Most existing LA segmentation methods work on ECG-gated CT or MRI data, where the boundary between the LA and the surrounding tissues is sufficiently clear to facilitate the segmentation. There is only one reported work on LA segmentation on nongated C-arm CT [7]. To handle the severe imaging artifacts of C-arm CT (e.g., cardiac motion blur), it also uses a model-based approach to exploit the prior shape information to improve segmentation robustness. Using a single holistic shape model to initialize the LA segmentation, Manzke *et al.*'s method [7] has difficulty to handle anatomical variations of the PVs, e.g., the left common PV and extra right middle PVs. The right middle PVs are completely missing in their LA model. For comparison, our approach can handle the left common PVs naturally (as shown in Fig. 12) and has the capability to extract right middle PVs (as shown in Fig. 13). Different to ours, the LA model of [7] does not include the LA appendage. Although the LA appendage itself is less important than the PVs in the catheter based ablations, the ridge between the LA appendage and the LSPV is an important ablation region. Including the LA appendage into the shape model provides better visual guidance for physicians to ablate the ridge.

In general, it is risky to directly compare segmentation errors reported in the literature due to the difference in imaging modalities, datasets, LA models, and error metrics, etc. A mean error of 1.31 mm was reported on a small C-arm CT dataset (33 patients) in [7] without including the challenging LA appendage in the model. Their surface-to-surface error does not include the part labeling error either. In our case, for a mesh part, we measure the distance to the corresponding part in the

TABLE III
QUANTITATIVE EVALUATION OF RIGHT MIDDLE PULMONARY VEIN EXTRACTION ON 140 DATASETS (70 LARGE X-RAY PANEL DATA AND 70 SMALL X-RAY PANEL DATA)

	Mesh Error (mm)				Vessel-Wise Evaluation	
	Mean	Std	Median	Max	Detection Rate	False Positives
Large Volumes	1.32	0.69	1.26	15.54	43/49 (87.8%)	3
Small Volumes	1.07	0.84	0.88	11.78	34/39 (87.2%)	5

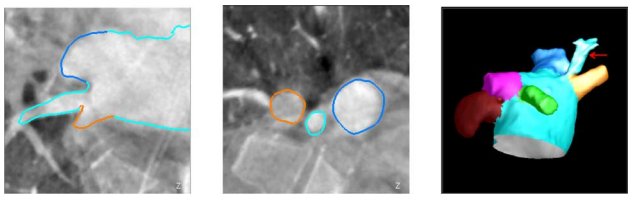

Fig. 13. Right middle pulmonary vein extraction result on a volume. The left two columns are two orthogonal views and the right column shows a 3-D visualization of the mesh (with the right middle pulmonary vein indicated by a red arrow).

ground truth; therefore, both the segmentation and mesh part labeling errors are penalized. To make a more direct comparison, the row "*Whole Mesh (No Part Label)*" in Tables I and II reports the similar error without considering the part label. That means the closest point is searched on the whole mesh (when we calculate the mesh error), not restricted to the part with the same label. The LA appendage can be further excluded as reported in row "*Whole Mesh (No Part Label + No LAA)*" of Tables I and II. Under this condition, we achieve a mean error of 1.25 mm and 1.23 mm for the large and small volumes, respectively. These errors are comparable to the 1.31 mm mean error reported in [7]. Since their evaluation was performed only on 33 patients from a single clinical site, it is not clear if sufficient anatomical variations are included in their small evaluation dataset (especially patients with left common PVs). Our method has been evaluated on a much larger dataset with 687 volumes from 18 clinical sites. It is more challenging to achieve accurate segmentation on a large heterogeneous dataset.

Except [7], previous methods on LA segmentation were tested on either CT or MRI data. Because of the higher image quality of CT and MRI, the segmentation errors are generally smaller than our results on C-arm CT data. For example, Kutra *et al.* [11] reported a mean mesh error of 1.1 mm on MRI data (0.72–2.0 mm volume resolution) and Cristoforetti *et al.* [19] achieved a mean error of 1.2 mm on CT data (0.8 mm volume resolution). However, the difference to ours is small. The current state-of-the-art CT scanner can acquire a 3-D volume with a resolution of 0.3–0.5 mm. Much smaller segmentation errors (0.53 mm) are reported in [21], [22] on such high resolution CT data.

B. Computational Complexity

The proposed method is computationally efficient. The whole segmentation procedure (including right middle PV extraction) takes about 2.6 s (on a computer with two Intel Xeon X5650 2.66 GHz CPUs, each with six cores) to process a volume with $256 \times 256 \times 245$ voxels. It compares favorably with the previous methods, e.g., 5 s in [23], 5–45 s in [5], 30 s in [7], and more than 2 h in [24].

C. Imaging Modalities

Previously, conventional CT or MRI is often used for surgical planning and visual guidance for transcatheter ablation of atrial fibrillation. As a new emerging image modality, C-arm CT has a few advantages over CT or MRI even though its image quality is generally lower. 1) It is more convenient to capture both 3-D (i.e., C-arm CT) and 2-D images (i.e., real-time fluoroscopy) from the same device, therefore saving time and cost to schedule a separate scan with CT or MRI. 2) Overlay of the 3-D LA model extracted from C-arm CT to 2-D fluoroscopy is straightforward using the intrinsic machine coordinate system. On the contrary, bringing a 3-D LA model extracted from CT or MRI to fluoroscopy is complicated, demanding extra manual interaction and time. 3) Last but not least, C-arm CT captures the current up-to-minute patient's physiological status. Conventional CT or MRI is often scanned days or even weeks before the intervention with different patient configurations, which incur extra changes of the LA shape and its relative position to other anatomies, e.g., the esophagus. Atrial-esophagus fistula is a serious complication of ablation, which often results in the death of the patient. Intra-operative C-arm CT provides more accurate delineation of the relative position the esophagus to the LA than preoperative CT or MRI. (Automatic esophagus segmentation from C-arm CT is part of our future work to enhance the current LA model.)

D. Limitations and Future Work

In this work, we use the surface curvature to define the boundary between the LA and PV. However, the transition from the LA to a PV is smooth both structurally and functionally. The myocardium muscular sleeve may extend from the LA into a PV up to 25 mm [44]. Ideally, the ablation strategy should be adapted to the thickness and length of the muscular sleeve of a patient. For example, more energy should be delivered to the region with a thick muscular sleeve. However, the muscular sleeve is ignored in current ablation practice due to the difficulty to delineate it using a noninvasive imaging modality. The muscular sleeve is an important source of ectopic electrical activity causing paroxysmal atrial fibrillation. The LA model presented in this work is mainly for the planning and visual guidance of ablation. To use the model for computational simulation of atrial arrhythmia, the LA myocardium (including the muscular sleeve) should be added.

In our current implementation, the left common PV is labeled as part of the LA chamber [Fig. 3(b) and Fig. 12(c)]; therefore, our method does not tell if the patient has a variation of the left common PV. In comparison, the method proposed by Kutra *et al.* [11] can potentially identify the anatomical variation pattern of the left PVs.

The major limitation of a model based segmentation approach is in handling rare anatomical variations. Our LA model does not include potential middle PVs on the left side. Technically, it is possible to adapt the middle PV extraction algorithm presented in Section V on the left side too. However, the current algorithm is not perfect and false positive detections may be generated. Since extra left middle PVs are extremely rare [8], we decide to exclude them. As another rare variation, a PV may drain into the top of the LA. Such a variation cannot be handled by the proposed method either.

Our LA model does not include the side branches of a PV since the AF ablation is normally performed around a PV ostium on the LA chamber surface. To the best of our knowledge, no physician performs ablation into a PV. Presence or absence of a side branch does not change the ablation strategy. Therefore, our LA model is sufficient to provide visual guidance for ablation. However, side branches may improve the aesthetic effect of the 3-D visualization, making the extracted LA model more realistic to physicians. Some physicians may prefer to have first-order side branches included in the model.

Anatomical variations are common in many human anatomies. For example, in the most common configuration, the aortic arch has three great vessels originating separately from it. Alternatively, two of the vessels may merge together before joining the aortic arch [45], which is similar to the variation of the left common PV. The proposed part based segmentation approach can also be applied to handle such anatomical variations.

VIII. Conclusion

We proposed a part based model for automatic segmentation of the LA (including chamber, appendage, four major PVs, and right middle PVs) in C-arm CT volumes, which can handle anatomical variations elegantly. Extensive experiments on 687 nongated C-arm CT datasets demonstrated the robustness and efficiency of the proposed method. The automatically extracted personalized LA model can help physicians to adapt a generic ablation strategy to a patient's specific anatomy. The LA model, together with marks of the adapted ablation strategy, can also be overlaid onto 2-D fluoroscopic images to provide visual guidance during the intervention procedure. Our system is retrainable, therefore can be extended to different medical imaging modalities, e.g., MRI and conventional CT.

Acknowledgment

The authors would like to thank anonymous reviewers for their constructive comments. The authors would also like to thank their colleague Dr. R. Liao for integrating the proposed LA segmentation algorithm for clinical evaluation.

References

[1] G. V. Naccarelli, H. Varker, J. Lin, and K. L. Schulman, "Increasing prevalence of atrial fibrillation and flutter in the United States," *Am. J. Cardiol.*, vol. 104, no. 11, pp. 1534–1539, 2009.

[2] P. A. Wolf, R. D. Abbott, and W. B. Kannel, "Atrial fibrillation as an independent risk factor for stroke: The Framingham study," *Stroke*, vol. 22, no. 8, pp. 983–988, 1991.

[3] P. P. Kneeland and M. C. Fang, "Trends in catheter ablation for atrial fibrillation in the United States," *J. Hospital Med.*, vol. 4, no. 7, pp. E-1–E-5, 2009.

[4] A. D'Silva and M. Wright, "Advances in imaging for atrial fibrillation ablation," *Radiol. Res. Practice*, vol. 2011, pp. 1–10, 2011.

[5] M. John and N. Rahn, "Automatic left atrium segmentation by cutting the blood pool at narrowings," in *Proc. Int. Conf. Med. Image Comput. Comput. Assist. Intervent.*, 2005, pp. 798–805.

[6] R. Karim, R. Mohiaddin, and D. Rueckert, "Left atrium segmentation for atrial fibrillation ablation," in *Proc. SPIE Med. Imag.*, 2008, vol. 6918, pp. 1–8.

[7] R. Manzke, C. Meyer, O. Ecabert, J. Peters, N. J. Noordhoek, A. Thiagalingam, V. Y. Reddy, R. C. Chan, and J. Weese, "Automatic segmentation of rotational X-ray images for anatomic intra-procedural surface generation in atrial fibrillation ablation procedures," *IEEE Trans. Med. Imag.*, vol. 29, no. 2, pp. 260–272, Feb. 2010.

[8] E. M. Marom, J. E. Herndon, Y. K. Kim, and H. P. McAdams, "Variations in pulmonary venous drainage to the left atrium: Implications for radiofrequency ablation," *Radiology*, vol. 230, pp. 824–829, 2004.

[9] H. Lombaert, Y. Sun, L. Grady, and C. Xu, "A multilevel banded graph cuts method for fast image segmentation," in *Proc. Int. Conf. Comput. Vis.*, 2005, pp. 259–265.

[10] Y. Zheng, A. Barbu, B. Georgescu, M. Scheuering, and D. Comaniciu, "Four-chamber heart modeling and automatic segmentation for 3-D cardiac CT volumes using marginal space learning and steerable features," *IEEE Trans. Med. Imag.*, vol. 27, no. 11, pp. 1668–1681, Nov. 2008.

[11] D. Kutra, A. Saalbach, H. Lehmann, A. Groth, S. P. M. Dries, M. W. Krueger, O. Dössel, and J. Weese, "Automatic multi-model-based segmentation of the left atrium in cardiac MRI scans," in *Proc. Int. Conf. Med. Image Comput. Comput. Assist. Intervent.*, 2012, pp. 1–8.

[12] Y. Y. Boykov and M.-P. Jolly, "Interactive graph cuts for optimal boundary and region segmentation of objects in N-D images," in *Proc. Int. Conf. Comput. Vis.*, 2001, pp. 105–112.

[13] Y. Boykov and G. Funka-Lea, "Graph cuts and efficient N-D image segmentation," *Int. J. Comput. Vis.*, vol. 70, no. 2, pp. 109–131, 2006.

[14] Y. Zheng, T. Wang, M. John, S. K. Zhou, J. Boese, and D. Comaniciu, "Multi-part left atrium modeling and segmentation in C-arm CT volumes for atrial fibrillation ablation," in *Proc. Int. Conf. Med. Image Comput. Comput. Assist. Intervent.*, 2011, pp. 487–495.

[15] Y. Zheng, M. John, J. Boese, and D. Comaniciu, "Precise segmentation of the left atrium in C-arm CT volumes with applications to atrial fibrillation ablation," in *Proc. IEEE Int.Sym. Biomed. Imag.*, 2012, pp. 1192–1195.

[16] D. Yang, Y. Zheng, and M. John, "Graph cuts based left atrium segmentation refinement and right middle pulmonary vein extraction in C-arm CT," in *Proc. SPIE Med. Imag.*, 2013, pp. 1–9.

[17] M. E. Rettmann, D. R. Holmes III, J. J. Camp, D. L. Packer, and R. A. Robb, "Validation of semi-automatic segmentation of the left atrium," in *Proc. SPIE Med. Imag.*, 2008, vol. 6916, pp. 1–7.

[18] G. Nollo, A. Cristoforetti, L. Faes, M. Centonze, M. D. Greco, R. Antolini, and F. Ravelli, "Registration and fusion of segmented left atrium CT images with CARTO electrical maps for the ablative treatment of atrial fibrillation," in *Proc. Comput. Cardiol.*, 2004, pp. 345–348.

[19] A. Cristoforetti, L. Faes, F. Ravelli, M. Centonze, M. D. Greco, R. Antolini, and G. Nollo, "Isolation of the left atrial surface from cardiac multi-detector CT images based on marker controlled watershed segmentation," *Med. Eng. Phys.*, vol. 30, no. 1, pp. 48–58, 2008.

[20] C. Meyer, R. Manzke, J. Peters, O. Ecabert, R. Kneser, V. Y. Reddy, R. C. Chan, and J. Weese, "Automatic intra-operative generation of geometric left atrium/pulmonary vein models from rotational X-ray angiography," in *Proc. Int. Conf. Med. Image Comput. Comput. Assist. Intervent.*, 2008, pp. 61–69.

[21] R. Hanna, H. Barschdorf, T. Klinder, F. M. Weber, M. W. Krueger, O. Dössel, and C. Lorenz, "A hybrid method for automatic anatomical variant detection and segmentation," in *Proc. Funct. Imag. Model. Heart*, 2011, pp. 333–340.

[22] P. Neher, H. Barschdorf, S. Dries, F. M. Weber, M. W. Krueger, O. Dössel, and C. Lorenz, "Automatic segmentation of cardiac CTs—Personalized atrial models augmented with electrophysiology structures," in *Proc. Funct. Imag. Model. Heart*, 2011, pp. 80–87.

[23] R. Karim, C. Juli, L. M. Lawes, P. Kanangaratnam, D. W. Davies, N. S. Peters, and D. Rueckert, "Automatic segmentation of left atrial geometry from contrast-enhanced magnetic resonance images using a probabilistic atlas," in *Proc. MICCAI Workshop Statist. Atlases Computat. Models Heart: Map. Structure Funct.*, 2010, pp. 134–143.

[24] M. Depa, M. R. Sabuncu, G. Holmvang, R. Nezafat, E. J. Schmidt, and P. Golland, "Robust atlas-based segmentation of highly variable anatomy: Left atrium segmentation," in *Proc. MICCAI Workshop Statist. Atlases Computat. Models Heart: Map. Structure Funct.*, 2010, pp. 85–94.

[25] R. Karim, D. R. R. Mohiaddin, and P. Drivas, "Automatic extraction of the left atrial anatomy from MR for atrial fibrillation ablation," in *Proc. IEEE Int. Sym. Biomed. Imag.*, 2009, pp. 502–505.

[26] A. Darge, M. R. Reynolds, and J. J. Germano, "Advances in atrial fibrillation ablation," *J. Invasive Cardiol.*, vol. 5, pp. 247–254, 2009.

[27] C. Wachinger and P. Golland, "Spectral label fusion," in *Proc. Int. Conf. Med. Image Comput. Comput. Assist. Intervent.*, 2012, pp. 410–417.

[28] L. D. Biase *et al.*, "Left atrial appendage: An underrecognized trigger site of atrial fibrillation," *Circulation*, vol. 122, no. 2, pp. 109–118, 2010.

[29] D. R. Holmes, V. Y. Reddy, Z. G. Turi, S. K. Doshi, H. Sievert, M. Buchbinder, C. M. Mullin, and P. Sick, PROTECT AF investigators, "Percutaneous closure of the left atrial appendage versus warfarin therapy for prevention of stroke in patients with atrial fibrillation: A randomized non-inferiority trial," *Lancet*, vol. 374, no. 9689, pp. 534–542, 2009.

[30] P. Grasland-Mongrain, J. Peters, and O. Ecabert, "Combination of shape-constrained and inflation deformable models with application to the segmentation of the left atrial appendage," in *Proc. IEEE Int. Sym. Biomed. Imag.*, 2010, pp. 428–431.

[31] M. Toews and T. Arbel, "A statistical parts-based model of anatomical variability," *IEEE Trans. Med. Imag.*, vol. 26, no. 4, pp. 497–508, Apr. 2007.

[32] O. Ecabert, J. Peters, M. J. Walker, T. Ivanc, C. Lorenz, J. von Berg, J. Lessick, M. Vembar, and J. Weese, "Segmentation of the heart and great vessels in CT images using a model-based adaptation framework," *Med. Image Anal.*, vol. 15, no. 6, pp. 863–876, 2011.

[33] Y. Zheng, B. Georgescu, and D. Comaniciu, "Marginal space learning for efficient detection of 2-D/3-D anatomical structures in medical images," in *Proc. Inf. Process. Med. Imag.*, 2009, pp. 411–422.

[34] P. Viola and M. Jones, "Rapid object detection using a boosted cascade of simple features," in *Proc. IEEE Conf. Comput. Vis. Pattern Recognit.*, 2001, pp. 511–518.

[35] T. F. Cootes, C. J. Taylor, D. H. Cooper, and J. Graham, "Active shape models-their training and application," *Comput. Vis. Image Understand.*, vol. 61, no. 1, pp. 38–59, 1995.

[36] B. K. P. Horn, "Closed form solution of absolute orientation using unit quaternions," *J. Opt. Soc. A*, vol. 4, no. 4, pp. 629–642, 1987.

[37] W. E. Lorensen and H. E. Cline, "Marching cubes: A high resolution 3-D surface construction algorithm," *Comput. Graph.*, vol. 21, no. 4, pp. 163–169, 1987.

[38] G. Taubin, "Optimal surface smoothing as filter design," in *Proc. Eur. Conf. Comput. Vis.*, 1996, pp. 283–292.

[39] M. Kass, A. Witkin, and D. Terzopoulos, "Snakes: Active contour models," *Int. J. Comput. Vis.*, vol. 1, no. 4, pp. 321–331, 1988.

[40] J. J. Moré and G. Toraldo, "On the solutions of large quadratic programming problems with bound constraints," *SIAM J. Optimizat.*, vol. 1, no. 1, pp. 93–113, 1991.

[41] D. J. Williams and M. Shah, "A fast algorithm for active contours and curvature estimation," *CVGIP: Image Understand.*, vol. 55, no. 1, pp. 14–26, 1992.

[42] Y. Boykov and V. Kolmogorov, "An experimental comparison of mincut/max-flow algorithms for energy minimization in vision," *IEEE Trans. Pattern Anal. Mach. Intell.*, vol. 26, no. 9, pp. 1124–1137, Sep. 2004.

[43] A. Thiagalingam, R. Manzke, A. D'avila, I. Ho, A. H. Locke, J. N. Ruskin, R. C. Chan, and V. Y. Reddy, "Intraprocedural volume imaging of the left atrium and pulmonary veins with rotational X-ray angiography: Implications for catheter ablation of atrial fibrillation," *J. Cardiovas. Electrophysiol.*, vol. 19, no. 3, pp. 293–300, 2008.

[44] S. Y. Ho, J. A. Cabrera, V. H. Tran, J. Farré, R. H. Anderson, and D. Sánchez-Quintana, "Architecture of the pulmonary veins: Relevance to radiofrequency ablation," *Heart*, vol. 86, pp. 265–270, 2001.

[45] K. F. Layton, D. F. Kallmes, H. J. Cloft, E. P. Lindell, and V. S. Cox, "Bovine aortic arch variant in humans: Clarification of a common misnomer," *Am. J. Neuroradiol.*, vol. 27, no. 7, pp. 1541–1542, 2006.